Smart Materials and Structures

PAPER • **OPEN ACCESS**

Effect of textile pre-stretch and printed geometry on the curvature of PLA-Lycra 4D textiles

To cite this article: Stefano Pandini *et al* 2024 *Smart Mater. Struct.* **33** 105023

OPEN ACCESS
IOP Publishing
Smart Materials and Structures
Smart Mater. Struct. **33** (2024) 105023 (20pp)
https://doi.org/10.1088/1361-665X/ad7800

Effect of textile pre-stretch and printed geometry on the curvature of PLA-Lycra 4D textiles

Stefano Pandini*, Chiara Pasini, Davide Battini, Andrea Avanzini, Antonio Fiorentino, Ileana Bodini and Simone Pasinetti

Department of Mechanical and Industrial Engineering, University of Brescia, 25123 Brescia, BS, Italy

E-mail: stefano.pandini@unibs.it

Received 26 June 2024, revised 19 August 2024
Accepted for publication 6 September 2024
Published 16 September 2024

Abstract

4D textiles are a specific class of 4D printed materials obtained by printing flat patterns on elastically pre-tensioned textiles and being able to switch from planar systems to complex 3D objects after the textile pre-stretch is released. The mechanical balance between textile recovering strain and printed structure stiffness determines the final shape. This study is carried out by coupling pre-stretched Lycra to PLA and explores ways to control 4D textile shape transformations by varying pre-stretch (10% ÷ 60%), printed structure geometry (bar-shaped and star-shaped elements; star-shaped patterns), printed element thickness (0.3 ÷ 3 mm) and mutual distance (2 ÷ 15 mm). By adjusting these parameters, a wide set of out-of-plane curvatures are obtained, ranging from flat, to dome-like and highly curved, wrapped or coiled shapes. Digital optical methods, including digital image analysis, 3D scanning, and digital image correlation, are used to evaluate the complexity of the final shape and strain state evolution during shape transformation. The geometry variation is measured in terms of height increase (maximum 45 mm for a star-shaped system, 30 mm for a multiple star pattern) and of area decrease (maximum 80% for a star-shaped system, 60% for a multiple star pattern). While most shape transformations occur immediately after printing ('direct 4D printing'), further shape evolutions may be triggered by heating above the PLA glass transition, allowing for the creation of dynamic structures whose shape changes upon external stimuli. The adhesion between the 3D printed element and the stretched textile is also examined, with a focus on determining the role of interfacial strength and the conditions that could enhance it. This study provides an overview of the primary design variables and valuable maps of their impacts on shape transformations in this broad scenario of influencing parameters.

Supplementary material for this article is available online

Keywords: 4D textiles, 4D printing, thermally activated transformation, self-assembly, adhesion

* Author to whom any correspondence should be addressed.

1. Introduction

4D printing is a novel processing approach that permits the easy and customised realization of objects with active response [1–4]. This is commonly done by additive manufacturing using materials that may change shape or properties over time (i.e. the 4th dimension) in reaction to environmental stimuli like temperature, electromagnetic field, humidity, or light. Smart materials like shape memory polymers [1, 2], smart composites [3, 4], and hydrogels [5] are used. Other methods use stress mismatch between layers printed with distinct anisotropic patterns or stresses created in polymers under certain printing conditions [6–9]. Thus, the obtained objects can change shape significantly in response to a stimulus, allowing complex or customised shapes or self-assembly or active response applications (adaptive medical implants [10, 11]; aircraft and architectural morphing panels [12]; soft robotics [13]).

4D textiles are a niche within the 4D printing scenario, with similar active responses to other 4D printed structures, but distinct operating principles and applications, and that may be summarized as 3D-printed planar sheets that can evolve into 3D structures. In the past, integrating textiles and fibres with solid materials was used to reinforce structures. However, recent research is now focused on developing innovative functional structures by combining these materials. This involves additional manufacturing processes to create self-assembly systems [14], which may revolutionise textile manufacturing [15] or the development of smart textiles [16], as well as taking advantage of the interactions between textiles and solid materials, in embedded [17] or multi-layer composite structures [18] to achieve specific features such as inherent shape memory or thermally activated shapeshifting abilities.

The 4D textile response is achieved by 3D printing a stiff material, usually beam-shaped reinforcements, onto elastically pre-tensioned textile fabrics, causing the printed part to bend and move out-of-plane and resulting in a rapid self-shaping process [19, 20].

Pre-stretching stores elastic energy within the textile and releasing the stretch transfers a part of this energy from the textile to the printed elements until an equilibrium configuration is reached. The mechanical balance between textile recovery stress and printed element elastic stiffness causes complicated curvature in constructed systems [19–23]. While the shape changes are typically driven by tension release from the textile [23], in some cases, a remote actuation of 4D textiles was also achieved by adopting stimuli-responsive materials, usually thermally activated [24–27].

4D textile production transforms planar patterns into three-dimensional shapes through folding, curling, bending, buckling, expanding, and shrinking, with equilibrium shapes including synclastic dome-shaped, anticlastic saddle, and double-curved surfaces.

The textile's out-of-plane deformation resembles biological systems like leaf folding or wrinkling [22] and Otto Frei's membrane structure [28], suggesting that 4D textiles can bring natural scientists, architects, and designers together to create bioinspired materials systems [29–31]. Possible applications regard smart textiles (shape-changing garments, self-transpiring textiles [25], sound-absorbing textiles [32], adaptive footwear [33], fashion garments or jewellery [34]), adaptive building materials (resilient architectural skins, shading dividers, large-scale temporary buildings or tents [35, 36]), and textiles for biomedical applications (smart bioprinted scaffolds [37], hybrid textiles with 3D printed stiffeners for the realization of orthopaedic devices with customised supporting areas [38]).

Since the textile should store energy like a spring, highly stretchable knitted fabrics like polyester elastane (Lycra, Spandex, Elaspan) can be employed [20, 39]. However, no precise requirements are set for the 3D printed part, and 4D textiles are commonly made using fused deposition modelling (FDM) of thermoplastics (PLA [21, 23, 25, 26], ABS [34]) or thermoplastic elastomers (TPU [25, 40]).

The stress state driving the responses of the final composite system is complex and influenced by mechanical properties of the components, tension applied to the textile, and the geometry and size of the printed elements. Importantly, the stiffness and the distribution of the printed material must guarantee the possibility of uncovered textile portions to retract upon pre-stretch release. By controlling the amounts of printed area and the pattern it is possible to achieve various types of deformation [20]. The thickness of the printed element also influences the shape and degree of curvature. To face the difficulties of programming the final 3D shape of 4D textiles, analytical and numerical modelling methods were also used, taking into account the many design variables and the complex behaviour of the materials, such as the textile's non-linear response under large strain and the printed material's multistable configurations [22, 23, 41].

The development of methods that print a planar design on a textile must also ensure adequate adhesion. Various methods have been investigated by researchers to improve the adhesion between the textile and the deposited polymer [42, 43]. Many studies concur that mechanical adhesion promotes adhesion more than chemical bonding [44, 45], thanks to a form-locking relationship between the polymer that penetrates the fabric's open-pore structure. Adhesion may thus be improved through textile structure and printing settings: on the textile side, adhesion may depend on knit parameters and fabric structure [44, 46], weave pattern and weft density [47], porosity and roughness [48], and stretching, since it controls fabric thread density [49]; technologically, it may be improved by a good combination of surface wettability, molecular diffusion, and pressure [49]; by properly adjusting the distance between the nozzle and the printing bed [50], the bed temperature [46, 50], and the printing speed, and by using flexible filaments [51, 52] and polymers with lower viscosity during printing [53, 54].

Research on 4D textiles is currently an underexplored area and while it provides valuable examples for both experimental [20–26] and simulated [22, 23] responses of these systems, the focus is often on experimental prototyping (e.g. table 2 in [15]). This limits our understanding of the driving principles for the morphing mechanism in self-shaping textiles.

Furthermore, the impact of design variables on the assumed final shape, particularly in cases of instability or multistability, has received limited attention [22, 23], primarily focusing on describing the effect in highly specific configurations within the vast design space.

To provide further knowledge, this study investigates the complexity of 4D textiles response and the correlation between design parameters (printed pattern shape and thickness, textile pre-stretch) and the final shape. Experiments were conducted on a commercial Lycra fabric, with two different PLA structures printed by FDM. Shape transformations were quantified using 3D scanners and strain measurements were performed using stereoscopic Digital Image Correlation. Statistical approaches (regression analyses together with ANOVA and AICc tests) were used to study the correlations between design parameters and changes in area and height. The study also investigated the possibility of thermally activating shape changes in a second moment with respect to pre-stretch release. Finally, the adhesion between the printed layers and the textile support was tested in 180° T-peel tests along the principal directions and for all the applied pre-tensions.

2. Experimental

2.1. Materials and specimen preparation

The 4D textiles were prepared by coupling two materials, a highly stretchable weft-knitted Lycra textile and a structure based on a poly(lactic acid) (PLA) filament suitable for FDM printing.

The textile was used as purchased, i.e. knitted only, and without any further treatments or pre-washing. The structural arrangement of the fabric is displayed in figure 1(a), highlighting the presence of series of loops (courses and wales) arranged along two main directions; the wale direction was labelled as 0°. The textile thickness, under no applied strain, was measured by means of a universal micrometer, and the average value on five specimens was 0.42 ± 0.005 mm.

The PLA filament (Raise3D PLA Premium) was purchased from Raise 3D Technologies, Inc. (Irvine, CA, United States). The filament has a diameter of 1.75 mm, and from the data sheets [55] it has a melting temperature of 150 °C and a melt flow rate of 7–11 g /10 min (measured at 210 °C under 2.16 kg). A 3D printer Raise3D Pro2 (Raise 3D Technologies) was employed, capable of FDM printing with thermoplastic resins. The FDM printer was equipped with a 0.4 mm nozzle and the nozzle temperature was set to 205 °C. The first layer was printed at a speed of 15 mm s^{-1}, while the remaining ones were printed at a speed of 60 mm s^{-1}. The printing plate was maintained at 60 °C (i.e. at PLA glass transition) to restrict PLA cooling and prevent premature solidification, aiming to improve PLA-textile adhesion [46]. Both the structures were obtained by printing radially symmetric elements, for which a radially symmetric infill was chosen.

Before printing, a biaxial state of stretch was applied to the textile, by stretching it equally along the two main directions (0° and 90°) and mounting it on a square frame, where it was held in place during printing (see figures 1(b)–(d), where the frame dimensions are also reported). By pre-cutting the fabric into squares of different dimensions, it was possible to vary the amount of stretch and obtain four different textile pre-stretch levels: approximately, 10%, 20%, 40%, and 60%. When mounting the fabric on the frame, first the four corners were fixed and then the midpoints of the sides. Care was taken to control the actual amount of stretch by marking the fabric in the non-stretched relaxed state and measuring the actual displacements of the markers and the overall elongation in the two directions after mounting the textile on the frame, verifying the approximate agreement with the desired deformation. While the central portion of the textile appeared biaxially stretched consistently with the intended deformation, a less homogenous strain state was present in proximity to the boundaries, where printing was therefore avoided. The frame was then taped to the 3D printer bed to secure it in a fixed position.

The software Solidworks (Dassault Systèmes, Vélizy-Villacoublay, France) was used to create the CAD models of the printed elements. Two designs, named '8-arm star' and '3-arm star pattern' were conceived and printed as shown in figures 1(e) and (f), respectively, along with details of their geometry. The slicing of the model was performed with a layer thickness of 0.15 mm by means of the software IdeaMaker (Raise 3D Technologies). The two designs were obtained with various geometry parameters: for the '8-arm star' configuration, the star shape and overall width remained unchanged, but the overall thickness was varied (thickness: 0.3, 0.6, 0.9, 1.2, 1.5 mm); for the '3-arm star pattern,' the number of star elements in the pattern, the star shape and overall width remained unchanged, while varying their thickness (0.3, 0.6, 0.9, 1.2, 1.5 mm) and the element mutual distance. As shown in figure 2(f) the mutual distance, or inter-distance (i.d.), was evaluated as the distance between the apex of an element arm and the closest element centre, and the three conditions explored, labelled as close, intermediate, and far, were realised for mutual distance values corresponding to 2 mm, 8.5 mm, and 15 mm, respectively.

After printing, the textile was removed from the printing plate and from the frame, so it was free to assume a 3D shape in response to the pre-stretch release.

In addition to the configurations described above, further specimens were realized. Preliminary tests were carried out by printing long bars (length: 80 mm; width: 5, 10, 20, 30 mm; thickness: 0.3, 0.6, 0.9 mm; 100%-dense ±45° infill) on pre-stretched textiles, to evaluate the correlation between textile pre-stretch, printed geometry and curvature achieved on simple shaped specimens. Additional test to study the strain state by Digital Image Correlation (section 2.4) were carried out on specimens prepared by monoaxial stretch (along 0°) of the supporting fabric.

Furthermore,'8-arms star' specimens with high thickness 3D printed element (thickness: 1.5, 2, 3 mm) were printed to evaluate the possibility of thermally triggering the shapeshifting abilities. These systems, after printing and being released

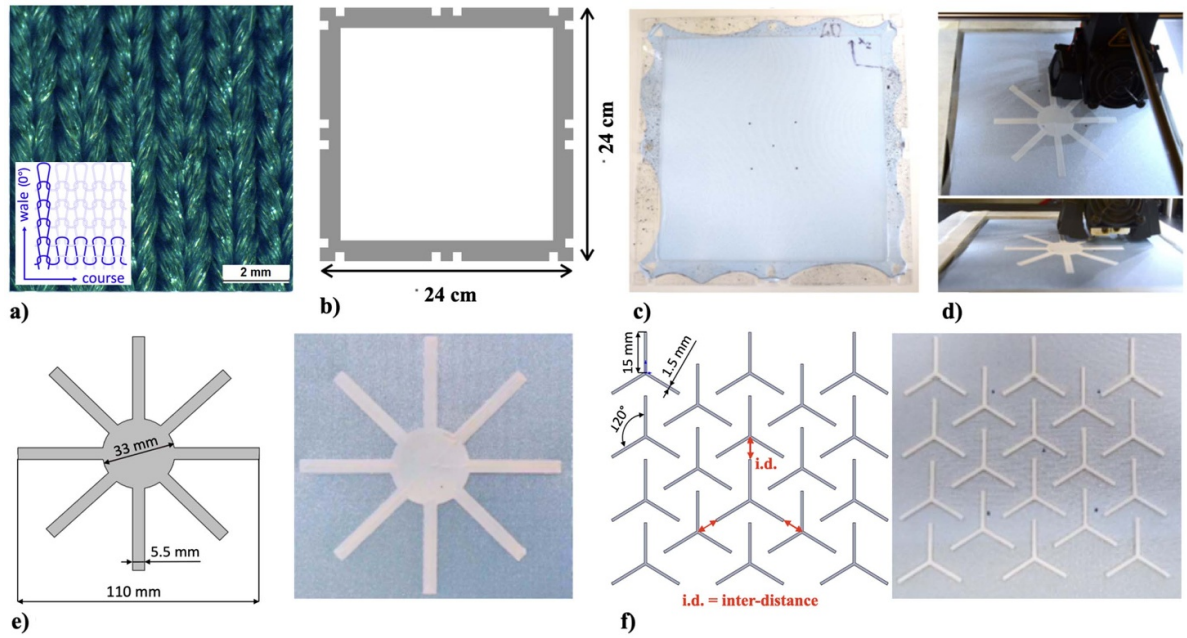

Figure 1. (a) Textile morphology and orientation; (b) frame for pre-stretch application; (c) pre-stretched textiles mounted on the frame; (d) printing on the pre-stretched textiles; (e) CAD and picture of the printed element in 8-arm star configuration and (f) 3-arm star pattern.

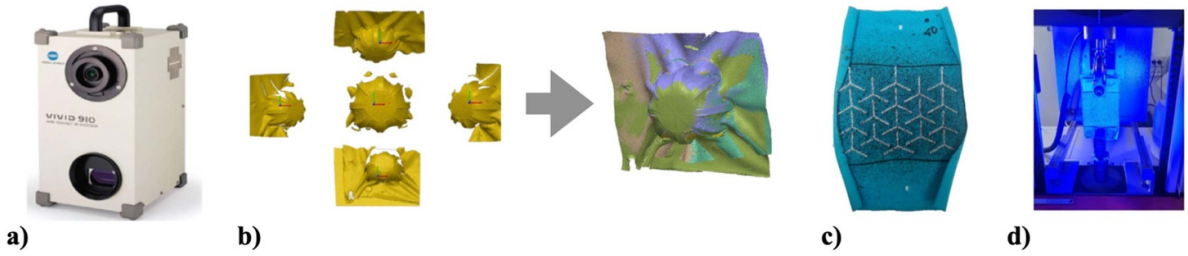

Figure 2. (a) 3D scanner; (b) 3D scan before and after re-alignment; (c) specimen for DIC test after sputtering; (d) DIC test configuration.

from the frame, were heated above the PLA glass transition temperature, by placing them in an oven at 80 °C for about 30 min. This allowed to reduce the PLA stiffness and further enhance the system curvature as an effect due to a change in temperature.

The change in the specimen shape was witnessed visually and recorded by means of a digital photo-camera. For bar specimens, the radius of curvature was measured. For 8-arm stars and 3-arm star patterns, different parameters were used. In fact, since the textile is known to have an anisotropic behaviour, although very limited for the pre-stretch values explored, it may exhibit different curvatures along the various directions; in addition, the structure of the 3-arm star pattern, lacking central symmetry, may also show different curvatures along the two main directions. To get a more accurate picture of the shapeshifting effect, the parameters used to measure the shape change are variations in the 3D printed element's projected area and height increase. These parameters were chosen over the main axes curvature (along the wall and course direction) or any other minor axis curvature. We evaluated the variation in the contour area of the printed zone, which is the top projection of the area that circumscribes the printed elements, as follows:

$$\text{area change } (\%) = \frac{A_{\text{after}} - A_{\text{in}}}{A_{\text{in}}} \times 100 \qquad (1)$$

where A_{in} represents the contour area measured on the tensioned samples, whereas A_{after} is measured on the sample after being released from the frame. The height increase of the printed area was measured using a tabletop as a reference for the lower base. Image analysis was performed using the software Image J.

2.2. Mechanical and thermal characterization

Tensile tests were carried out by means of an electromechanical dynamometer (Instron Mod. 3366) on both textile and printed PLA. Textile samples were rectangular strips cut from the fabric, with an overall length equal to 120 mm (gauge length, L_0: 100 mm) and width equal to 70 mm, larger than the

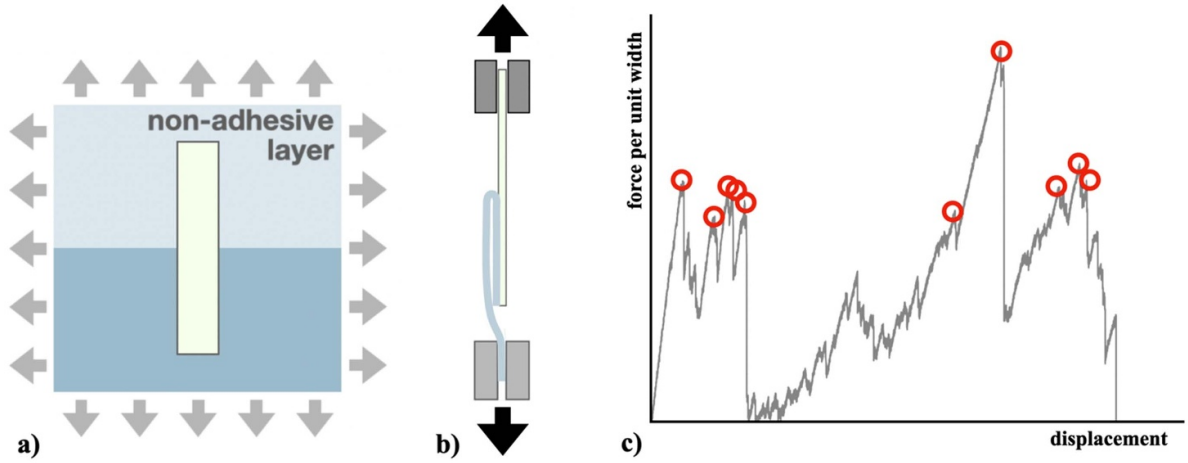

Figure 3. (a) Schematic representation of a) specimen preparation for peel tests and (b) peel test on a specimen gripped in the dynamometer; (c) schematic representation of typical results of a peel test, with the ten highest normalised force peaks highlighted.

clamp width (50 mm), so that the textile sample laterally overhang with respect to the clamps. The tests were performed up to final rupture with a crosshead speed equal to 100 mm min^{-1}; apparent nominal stress and strain were respectively evaluated as:

$$\sigma_{\text{app}} = \frac{F}{A} \tag{2}$$

$$\varepsilon_{\text{app}} = \frac{\Delta L}{L_0} \tag{3}$$

where F is the measured force, ΔL is the crosshead displacement, A is the specimen cross-section, and L_0 is the gauge length; stress and strain, calculated through normalization on cross-section and gauge length, are termed apparent due to the non-homogeneous nature and the complex micro-structure of the materials. Measurements were carried out along various directions (0°, 15°, 30°, 45°, 60°, and 90° with respect to the wale direction) to investigate the degree of anisotropy in the fabric, testing three samples for each direction.

Tensile tests on PLA specimens were carried out on printed tensile bars, with cross-section equal to 9 × 0.4 mm and overall length equal to 100 mm. The specimens were printed with different filament orientations: unidirectional samples had a structure in which all the filaments were deposed along the major axis of the specimen; multi-directional samples were printed with three different choices of infill main directions (i.e. with filaments at 0/90°, +45°/−45° and 60°/−30°). The tests were carried out at a crosshead speed equal to 10 mm min^{-1} and with a gauge length of 60 mm until failure. The apparent stress and apparent strain were evaluated according to equations (2) and (3).

Thermal characterization was carried out on PLA by means of Differential Scanning Calorimetry (DSC) and Dynamic Mechanical Thermal Analysis (DMTA).

DSC analysis was carried out on about 10 mg cut from the printed PLA bars. The thermal program involved a first heating at 10 °C min $^{-1}$ from −60 °C to 220 °C at 10 °C min^{-1}, followed by cooling to −60 °C and a second heating at 220 °C, all carried out at 10 °C min^{-1} .

DMTA tests were carried out on tensile bars (length between clamps: 20 mm; width: 5 mm; thickness: 1.5 mm). The tests were performed under tensile conditions, at a frequency of 1 Hz and on a heating ramp between 20 °C and 220 °C at 1 °C min^{-1}.

2.3. 3D scan

Measurements on the specimens have been ulteriorly validated thorough an optical non-contact technique. A 3D scanner was utilized to create precise and accurate three-dimensional reconstructions of the printed specimens. The main goal of adopting this scanning technique was to provide a more accurate assessment of the displacement of each point of the specimen in a direction perpendicular to the plane, with a specific focus on changes in height.

A Konica Minolta Vivid 910 3D scanner has been used (figure 3(a)). The Vivid 910 employs a laser scanner based on triangulation to capture three-dimensional data. The laser scanner is a laser emitter that projects a laser blade, which is deformed following the profile of the object to be scanned. A camera placed in triangulation with the blade acquires the latter's deformation and allows 3D measurement. Laser scanner technology offers several advantages such as (i) efficient capture of large amounts of data without physically touching the object, (ii) capability of capturing both the shape and texture of objects, and (iii) high accuracy and resolution. The used 3D scanner allows the acquisition of 24 bit full-colour images and gather approximately 300 000 points with an overall accuracy of 0.10 mm.

Typically, obtaining the complete 3D structure needs numerous scans from different perspectives. The analysed specimens usually underwent 3–5 scans to ensure accurate capture of all the elements of the structure. A single scan was adequate to acquire the necessary information for specimens that were generally flat. Each acquired point cloud has been then processed using Polygon Editing Tool (Polyworks®) software (figure 3(b)). This software helps to realign point clouds obtained from each scan. This stage guaranteed that

the reconstructed 3D model mirrored the original specimen. The Polygon Editing Tool software generated a 3D mesh of the scanned object, which was subsequently examined using SolidWorks. The point clouds exhibit good alignments, with alignment mean distances less than 0.1 mm. These values are deemed acceptable for the studied application, as the alignment accuracy is less than 1% of the change in sample size.

2.4. Digital image correlation

Digital Image Correlation analysis was carried out to assess the local strain evolution in the whole system during the shape transformation that occurs after release of stretching on monoaxially pre-stretched samples, with specific focus on the strain distribution in the vicinity of the printed regions. To slow down the shape transformation at stretch release, the tension was applied and slowly released by means of the electromechanical dynamometer (Instron mod. 3366) under uniaxial tensile configuration.

The measurements were conducted on specific specimens, including: 8-arm stars with a thickness of 0.3 mm and pre-stretch levels of 10% and 20%; 3-arm star patterns with thicknesses of 0.3 mm and 1.5 mm, intermediate distance of the pattern elements (i.e. mutual distance: 24 mm), and pre-stretch levels of 20%, 40% and 60%.

Prior to removing the sample from the frame, a rectangular shape was drawn on the cloth that was stretched over the frame, including the printed area, so to better control the stretch to apply in the dynamometer before the controlled stretch release and to accurately replicate the strain state during printing. Then, a black speckle-like pattern was sprayed to the samples using a basic spray can (figure 2(c)). Subsequently, the samples were extracted from the frame and precisely trimmed along the two longitudinal sides of the outside border, so to simplify their installation in the grips of the dynamometer.

The specimens were then mounted in the grip of the dynamometer and stretched along the pre-stretch direction so to recreate, approximately, the uniaxial stretched state of the sample when mounted on the frame and during printing. Finally, the stretch was reduced through the displacement of the crosshead at a controlled rate (20 mm min^{-1}), and the strain evolution was tracked through the DIC apparatus.

For the measurements, the GOM Aramis calibrated stereoscopic configuration device, which includes two 6 MP cameras (GOM Aramis 6 MP), two blue light sources, and polarised filters on each component, was used for these measurements. The stereoscopic recordings were analysed using the GOM-correlate 2020 software. The size of the facets in the 4D printed structural geometry ranged from 15 to 27 pixels, while the centre–centre distance varied between 9 and 13 pixels. These variations were determined by the size and quality of the speckle pattern.

The two cameras, configured in a stereoscopic setup, evaluated the movement of the speckle points to obtain the deformation field (figure 2(d)). The results were assessed using the primary reference system, which exclusively considers axial stress and elongational strain. The local strain state was quantified in terms of three main outputs: the minimal primary deformation field, the longitudinal deformation field in the direction of load application, and the displacement of the structure along the out-of-plane direction of the fabric.

2.5. Adhesion tests

A 180° delamination peel test methodology was employed to measure the degree of adhesion between the 3D printed material and the textile. The specimens for this evaluation were realized by printing bars (length: 80 mm; width: 10 mm; thickness: 3 mm) on pre-stretched fabric at different levels of biaxial pre-stretching (10%, 20%, 40%, 60%). The bars were printed with several orientations of their longitudinal axis with respect to the wale direction (0°, 45°, 90°). Half of the fabric was covered by a tape with non-adhesive side, as schematically depicted in figure 3(a), so to create a region of non-adhered interface between the fabric and half of the printed bar. These non-adhered extremities could be easily detached and clamped in the grips of an electro-mechanic dynamometer (Instron, Mod. 3366), the lower clamp securing the textile and the higher clamp securing the end of the printed bar (see figure 3(b)). By pulling the clamped extremities apart, as in a tensile test, it was possible to quantify the force required to separate the two adhered surfaces. The test was carried out at a crosshead speed equal to 5 mm min^{-1}, until full peeling, and repeated three times for each type of specimen.

A schematic representation of typical results of a peel test is depicted in figure 3(c) in terms of force normalised over the width of the printed PLA bar as a function of the crosshead displacement. Due to the discontinuous trend of these curves, the interface strength was arbitrarily expressed as the average of the top 10 peaks of normalized force, as highlighted in figure 3(c).

3. Results

3.1. Mechanical and thermal properties of 4D textile constituents

Both 4D textile constituents, i.e. Lycra textile and 3D printed PLA, were subjected to mechanical characterization, carried out under tensile conditions, and aimed at evaluating their mechanical response at small and finite strain. Both constituents present non-homogeneous morphology and anisotropic features, due to their structure formed by multiple, variously oriented, threads or filaments, respectively. For this reason, tensile tests were carried out along various directions with respect to either the wale direction (0°, see figure 1(a)), in the case of the textile, or the filament direction, in the case of the printed bars.

In the case of textiles, the apparent stress vs. strain curves, reported in figure 4(a), exhibit for all the directions a two-stage behaviour, characterised by a gradual transition from an initial more compliant response to a stiffer response at larger strains, where the curve divergence becomes particularly important.

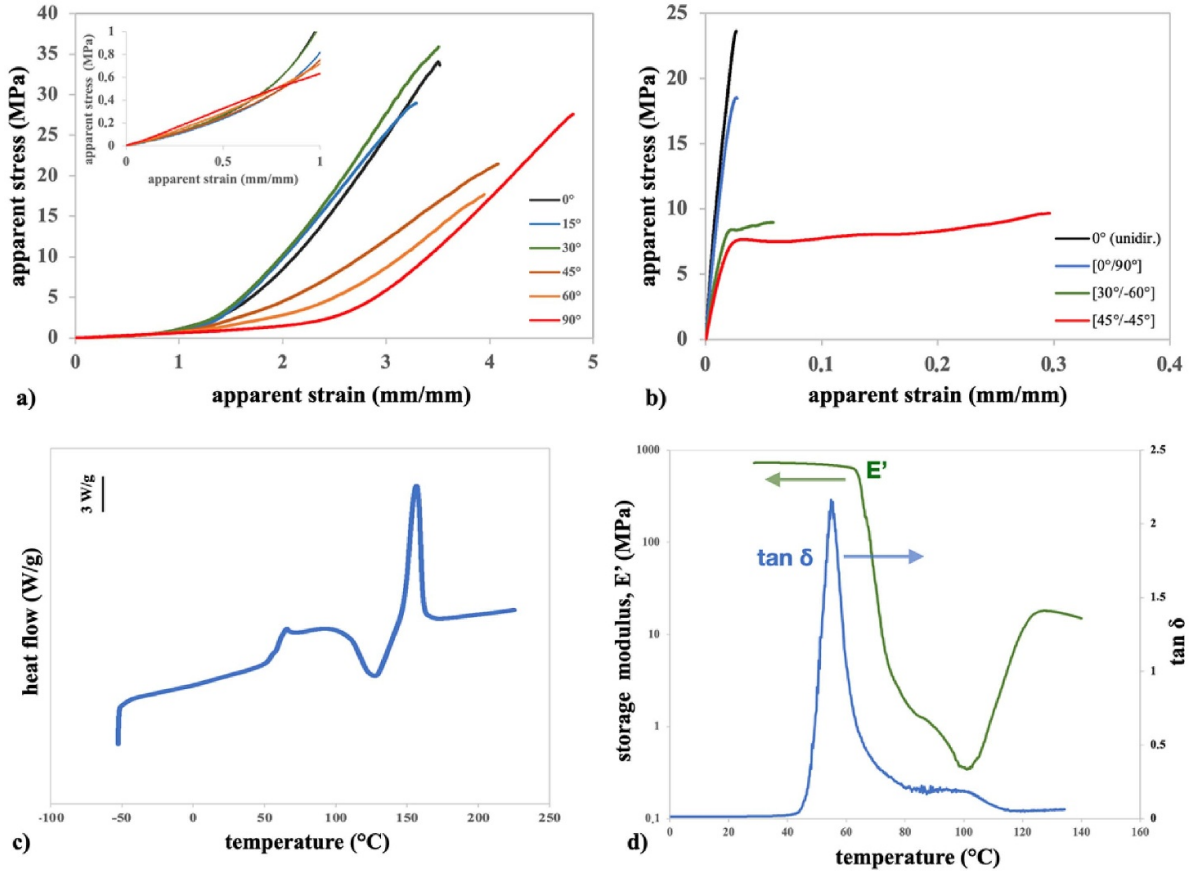

Figure 4. Apparent stress vs. apparent strain curves measured under tensile conditions for (a) Lycra textile specimens and (b) 3D printed PLA specimens tested along various directions (insert of figure 4(a): magnification of the first part of the curves)); (c) DSC and (d) DMA trace of samples obtained from PLA bars after printing.

This J-shaped type of curve guarantees high flexibility together with a good resistance to excessive deformation and is associated with a bending-to-stretching transition of the deformation mode under tension; such J-shaped stress-strain response is also found in many biological tissues, due to their curvy filamentary entangled microstructures, and shows potential for bio-integrated electronics or other flexible medical devices [56]. The apparent Young's modulus, E_{app}, in the first, more compliant, region was evaluated as average slope of the early linear part of the apparent stress *vs.* strain curve. A moderate dependence on direction is witnessed, with E_{app} changing between about 0.4 MPa, a value similarly shown by testing the materials at 0°, 15°, 30° and 45°, and increasing up to about 0.6 MPa, for larger angles up to 90°, as reported in table 1. While in the first part of the curve the fibres in the textile may easily stretch and deflect, in the second regime a stiffening effect occurs because of a remarkable tightening of the knitted fibre loops, above apparent strains of about 50%–200%, depending on the testing direction. The anisotropic response was found particularly relevant for these strain levels onwards: as the textile loops become tighter, fibres tend to align especially along the wale direction, leading to higher stress and lower strain at break for loading direction up to 30°, and failing at lower stress and larger strain for loads applied at higher angles. Since for high strain it is expected a large difference in the textile structure and mechanical behaviour along the various directions, no pre-stretch above 60% was applied in this study.

The properties of printed PLA were investigated on bars that were prepared with unidirectional filament deposition along the specimen longitudinal axis (0°), which are representative of the bar segments constituting the arms of stars in the various printed structures due to their concentric infill. In addition, to better highlight the effect of possible anisotropy in other typical 3D printed arrangements, tensile tests were carried out on specimens printed with various orientations of grid infill, i.e. alternating two orthogonal filament directions in successive layers according to the following stacking sequences: [0°/90°], [−60°/30°], and [±45°]. The results are reported in figure 4(b) and in table 1.

An anisotropic response of the system was found also in this case, and as expected systems with filaments at 0° show the maximum stiffness, of about 1.2 GPa, becoming about half for the [−60°/30°] system, and one-third for the [±45°] one. The slight difference in stiffness between the 0° unidirectional system and the [0°/90°] is ascribed to the porosity of the structure, whereas at higher angles the effect is due to the filament direction. The presence of 90° filaments lead to a strength reduction, and a further reduction is shown for the [−60°/30°] and [±45°] stacking sequences. A brittle behaviour is found for

Table 1. Apparent young's modulus, ultimate stress and ultimate strain for textile specimens and printed PLA specimens tested under tension along various directions.

Textile				PLA			
Direction	Young's modulus (MPa)	Ultimate stress (MPa)	Ultimate strain (mm mm^{-1})	Direction	Young's modulus (MPa)	Ultimate stress (MPa)	Ultimate strain (mm mm^{-1})
0°	0.39 ± 0.01	32 ± 3	3.50 ± 0.03	0° (unidir.)	1200 ± 140	26 ± 3	0.030 ± 0.004
45°	0.40 ± 0.06	19 ± 2	4.0 ± 0.1	[0°/90°]	1130 ± 160	18 ± 2	0.026 ± 0.001
60°	0.46 ± 0.04	21 ± 3	4.2 ± 0.3	[30°/−60°]	640 ± 160	10 ± 1	0.04 ± 0.02
90°	0.609 ± 0.003	24 ± 7	4.8 ± 0.1	[45°/−45°]	360 ± 40	13 ± 3	0.36 ± 0.07

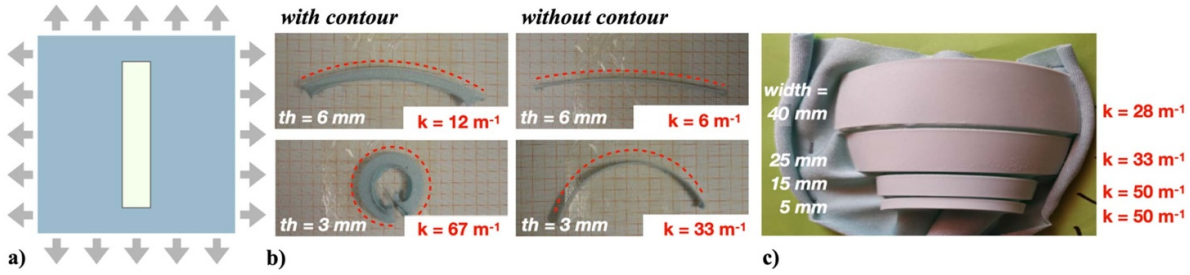

Figure 5. (a) Schematic representation of how preliminary 4D printed specimens were prepared; (b) specimen curvature and curvature values (k) for different PLA thicknesses, with and without textile contour (pre-stretch = 100%; PLA width = 5 mm); (c) specimen curvature and r values for various PLA widths (pre-stretch = 60%; PLA thickness = 0.9 mm).

most of the systems, while only the [±45°] system shows larger strain at break.

Overall, the results of the mechanical characterization reveal that all the systems exhibit much higher stiffness, comparable strength, and much lower deformation at break than the textile; still, a low thickness of printed PLA elements shall guarantee sufficient flexibility of 4D textiles. The most important mechanical difference regards the stiffness of the two constituents, which differ of about three orders of magnitude. In the assembled structure, PLA acts as the stiffer component and the textile as highly stretchable and compliant substrate. With respect to this remarkable stiffness mismatch, anisotropy effects may be considered less relevant, and they are further limited in this work by selecting textile pre-stretch levels within 60% and a concentric infill for the arms of the stars.

The thermo-mechanical properties of PLA were also tested by means of DSC and DMTA after 3D printing. DSC tests are represented in figure 4(c) as 1st heating scan trace of the printed element, which better represents the element condition right after printing. The thermogram shows a glass transition temperature, $T_g \approx 60$ °C, followed by a cold crystallization with peak at 128 °C, and a melting transition at 153 °C. The similar values of enthalpy associated to the cold-crystallization and melting peaks revealed that the material is fully amorphous after being printed and let cool down. The dynamic mechanical thermal analysis results are displayed in figure 4(d) as storage modulus and tan δ traces, for tests carried out on a printed bar. Storage modulus curve shows a significant stiffness reduction across the glass transition region, in proximity to the tan d peak, and approaches a rubbery modulus of about 1 MPa at 80 °C. A further modulus reduction is found at higher temperatures, until the recrystallization process, onsetting at 100 °C, leads to a later modulus increase.

3.2. Preliminary testing of the 4D textiles behaviour

A preliminary observation of the 4D textiles behaviour was attempted on specimens with simplified shape in order to better guide the choice of realization parameters in combining the two materials, such as the pre-stretch of the textile and the thickness of printed PLA elements. The specimens were prepared, as sketched in figure 5(a), by applying various biaxial pre-stretch values to the textile and printing PLA bar-shaped elements, with various thickness and width values, along the wale direction (i.e. 0°).

As a consequence of the equilibrium achieved after removing the printed system from the frame, the material undergoes a certain curvature, determined by the pre-stretch level and by the difference in elasticity of the two materials: the textile works in fact as a spring, undergoing contraction due to elastic recovery, while PLA serves as a stiffening agent to oppose the contraction and thereby guide and control the final curvature, as shown in the examples in figures 5(b) and (c). The material response was expressed in terms of average curvature (k) measured on photographs of the specimens.

Thickness and pre-stretch have an important influence on curvature, which increases with pre-stretch and decreases with thickness of the printed PLA; consequently, lower values of the radius of curvature are found for higher textile pre-stretch and lower PLA thickness.

However, the results unequivocally demonstrated also that the curvature obtained was markedly affected both by the presence of the textile contour surrounding the printed area and by the width of the specimen. In fact, when the surrounding contour is fully trimmed out of the specimen, the curvature is seen to decrease this is very well visible in the two examples in figure 5(b), in which this effect is particularly enhanced by

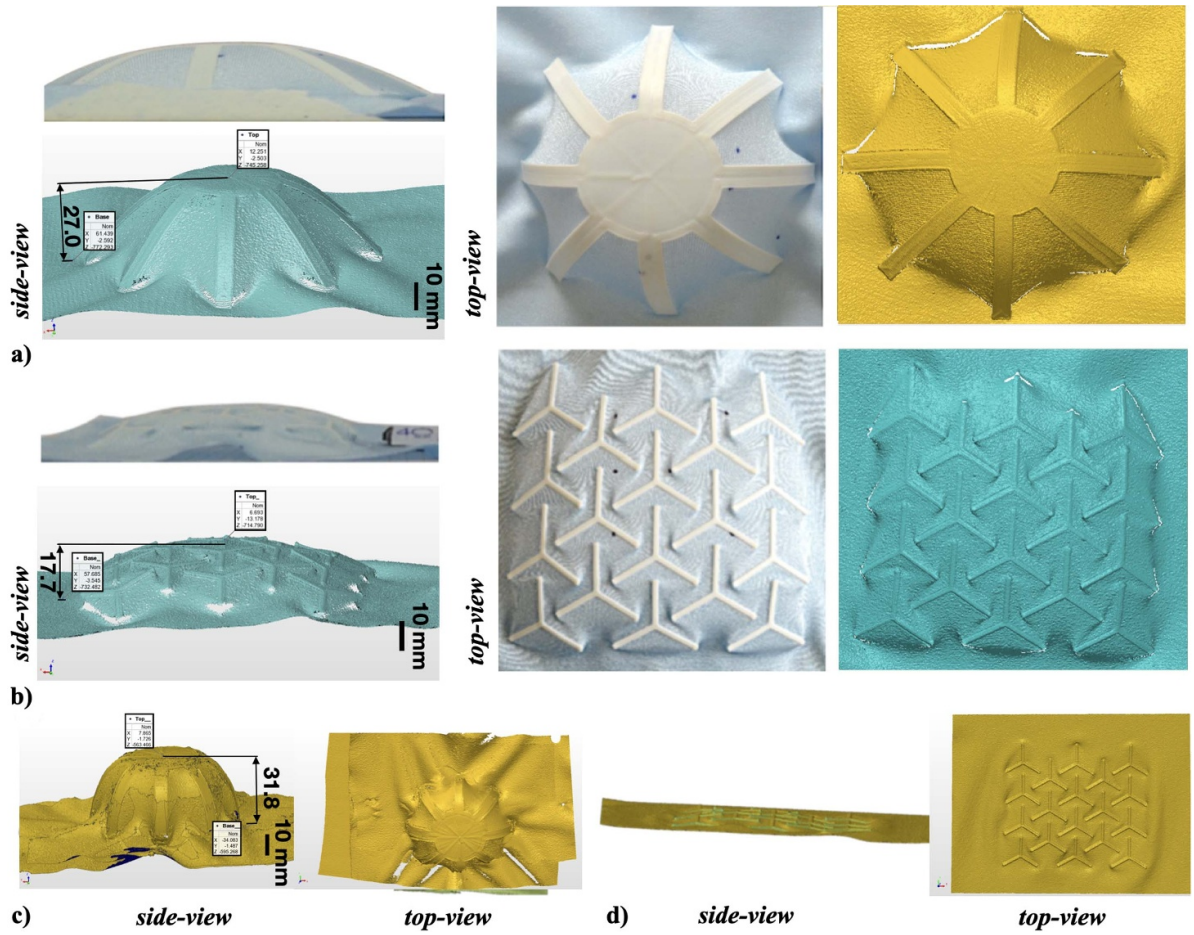

Figure 6. Pictures and 3D scans of the configurations displayed by the 4D textiles after printing and removing from the frame for (a) 8-arm star configuration, thickness: 0.9 mm, pre-stretch: 40%; (b) 3-arm star pattern, thickness: 0.9 mm, pre-stretch: 40%, mutual distance: intermediate. Measured distances are expressed in mm.

adopting a high pre-stretch of 100%. Furthermore, as shown in figure 5(c), the results change when printing specimens with same thickness (0.9 mm) but different width values, on a textile with a same pre-stretch (60%); in fact, a more pronounced curvature is obtained for specimens with lower width, suggesting an enhancing effect when in presence of a larger contour length/printed area ratio.

All this evidence indicates that, in addition to the stress at the interface between the textile and printed elements, the stress accumulated in the surrounding area also exerts a significant influence. Consequently, the two geometries under study, the 8-arm star configuration and the 3-arm star pattern, were properly designed to gather significant amounts of stretched textile around the printed regions.

3.3. Transformation of the 4D textiles

The typical final shapes of the two geometries investigated, quickly gained after printing and removal from the frame, are reported in figure 6, both as photographic images and as 3D scans. The first examples, an 8-arm star configuration (figure 6(a)) and a 3-arm star pattern (figure 7(b)), are chosen from the most regular shapes displayed by the two systems. Both images illustrate that when the stretch is released, the structures typically reconfigure in a curved dome-like shape, allowing a shift from a two-dimensional configuration to a three-dimensional structure. The shape transformation upon stretch release involves the bending of the printed portions. The shape assumed strongly depends on the geometry under investigation, and the resultant curvature value is greatly affected by the interplay between the thickness of the PLA and the pre-stretching of the cloth. In fact, depending on the specific conditions, the results can vary from remarkably high curvature values (e.g. 3D scans in figure 6(c)) to completely flat structures, when no overall change is detected (e.g. 3D scans in figure 6(d)).

The strain state evolution upon shapeshifting was studied by using digital image correlation, on textiles that were uniaxially pre-stretched before printing and for which the 4D textile recovery was intentionally slowed down at a controlled rate by means of the motion of the crosshead of a uniaxial dynamometer. From the initial state, where the fabric was fully stretched, the specimen was unloaded until a final state where the measured load reached zero. The DIC analysis allows for the extraction and computation of many field quantities and three of those were chosen to represent the specimen

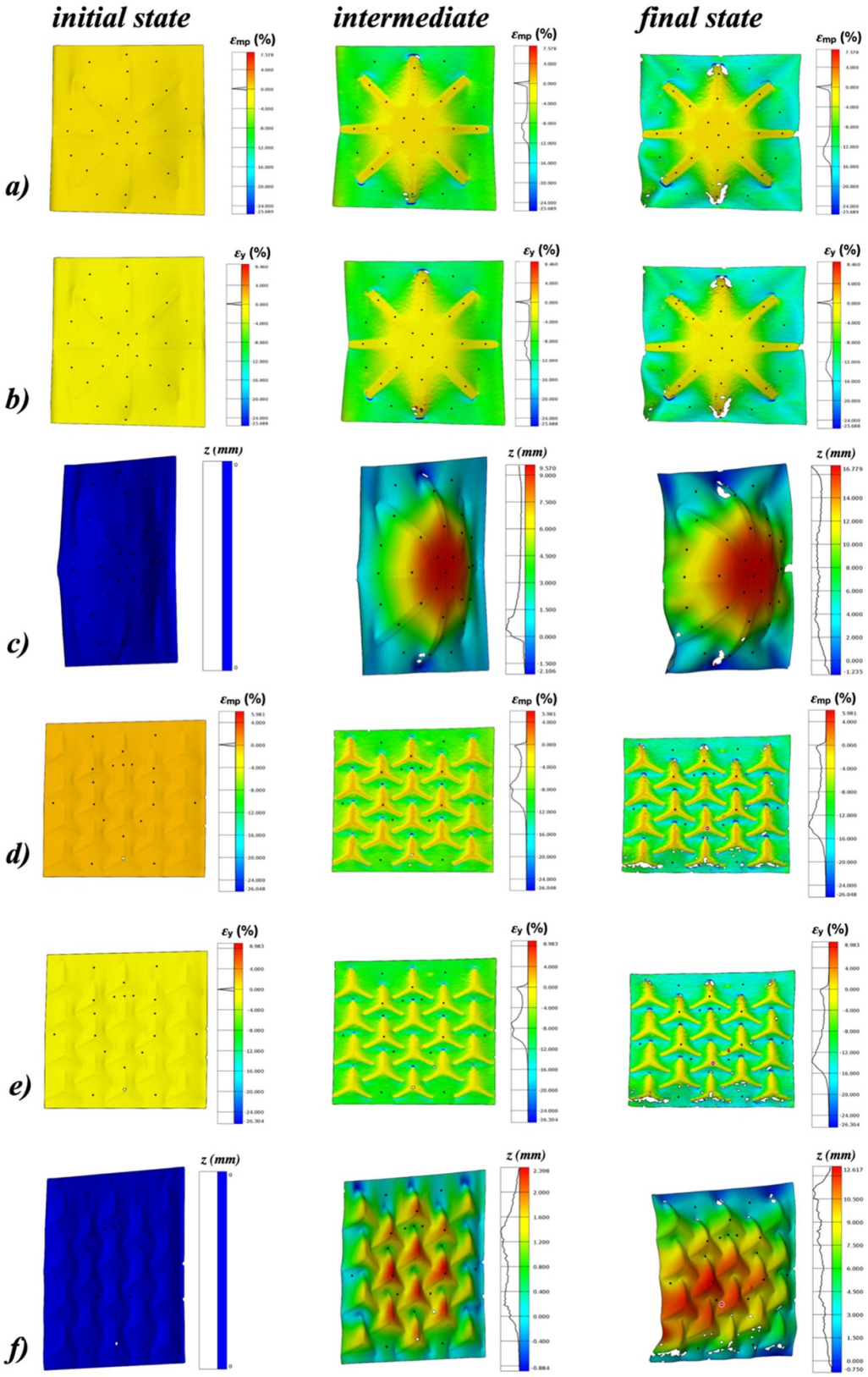

Figure 7. Evolution of the strain state upon three different recovery moments (1st picture: initial state, i.e. fully stretched; 2nd picture: intermediate state; 3rd image: final state) in terms of the minimum principal strain, ε_{mp} (a), (d), the strain component along y, ε_y (b), (e), and the out-of-plane displacement, z, along z direction (c), (f). Sets (a)–(c) refer to an 8-arm star specimen, (d)–(f) to a 3-arm star pattern with intermediate element inter-distance, both with printed thickness equal to 0.3 mm and pre-stretch equal to 20%.

evolution during the test: the minimum principal strain, the strain component in the y-direction (i.e. the loading direction) and the displacement in the z-direction (i.e. out of plane). These quantities were represented both in terms of field maps, to appreciate local values and gradients at a given time during the transformation and plotted as a function of the crosshead displacement for a user-defined set of n locations, to easily check pointwise their evolution during the shape change. On a side note, the minimum principal strain was chosen over the maximum principal strain because the recording starts with the specimen in a maximally stretched condition (hence this is an unloading test) and evolves towards the undeformed condition.

The field maps are reported in figure 7 for two selected samples (figures 7(a)–(c): 8-arm star specimen, thickness: 0.3 mm, pre-stretch: 20%; figures 7(d)–(f): 3-arm star pattern, thickness: 0.3 mm, pre-stretch: 20%), showing the three output parameters for three different moments of the shape-shifting process: i) the initial state, where the fabric is fully stretched; ii) an intermediate state of the shape-shifting process and iii) the final state, where all the applied stretch is recovered and no external load is applied. The picture shows the distribution of the plotted quantity (minimum principal strain, ε_{mp} (a, d); strain component along y, ε_y (b, e); out-of-plane displacement along z direction, z (c, f)), within the measurement area, both as scale of colour and in the scale plot close to each map. The selected points for which the full time-history of local strain values was reconstructed are shown as black dots.

Supplementary materials include additional pictures for further configurations (figures S1–S5), as well as two videos of the full test sequence (Mov 1 for the 8-arm star and Mov 2 for the 3-arm star pattern of figure 7).

The state of strain, as detected using digital image correlation, exhibits a widespread area of strain across the components, and it enables the identification of distinct regions in terms of strain. In fact, in all the examined specimens, the recovery of the textile pre-stretch is opposed by the stiff printed elements, so that the printed regions undergo changes in curvature with minimal deformation (a typical behaviour of pure bending in thin solids), whereas non-printed areas of the textile are less constrained and exhibit progressive deformation. Scale plots close to the pictures of figures 7(a), (b), (d) and (e) clearly highlight this bimodal distribution in the minimum principal strain and in the strain along the y-axis, as identified by two distinct peaks: one at zero strain and one that decreases progressively, reaching values of about -13% in the final state; these final values vary proportionally to the initial pre-stretch. Regarding the displacement along the z-axis (figures 7(c) and (f), the distribution solely pertains to macroscopic shape evolution of the specimen caused by its curvature.

Moreover, the black dots shown in figure 7, and mapped for better comprehension in figure 8, were probed to record their evolution upon the 4D textile transformation. Their locations were selected to collect data in regions affected by the peak minimum principal strain and the peak out-of-plane displacement (z-direction), as well as some regions in between to achieve a fair coverage of the whole measuring area.

The minimum principal strain trend against the maximum out-of-plane displacement is represented in figure 8, where the points are arranged in three main groups: points belonging to the fabric (black curves); points on the printed polymer (cyan curves); points at the singular areas near the printed polymer-textile boundaries (pink and orange curves). A picture and a scheme for the interpretation of the dots-curves correspondence is also present.

All points located on top of the printed polymer structure (cyan curves) show an almost flat trend of the minimum principal strain due to the polymer being very thin and much stiffer than the fabric leading to the activation of a small-strain membrane-like bending behaviour. On the other hand, the black curves, representing generic points on the fabric, which exhibits a very low stiffness, show high deformation levels, and undergo a progressive stretch recovery as the transformation occurs; the strain decreases linearly with the maximum out-of-plane displacement, until the specimen is basically undeformed, and a plateau strain is reached. Interestingly, the strain values and trends are similar for all the black points of each specimen, suggesting for the 8-arm star specimen a central symmetry behaviour, and for the 3-arm strain pattern the presence of a homogenous strain field in all the fabric areas trapped between the various elements; these observations are useful in attempting a description of the response of a very complex strain field. Finally, the pink and orange curves, which refer to the singularity regions at the polymer-fabric border along the stretching direction, display a behaviour similar to what can be seen for non-singular fabric regions (black curves), with the deformation decreasing as the tension decreases (and the out-of-plane displacement increases) and then reaching a plateau when the specimen is almost unloaded, but contracting at a higher rate and approaching the largest strain values. In fact, upon release, a rapid decrease of strain is seen to localize on the points located on singular fabric regions and acting axially, contributing as an eccentric stress condition to the specimen curvature. This behaviour can be attributed to the stiffness discontinuity located in the most stretch sensitive area of the specimen, where the polymer shape strongly inhibits the main strain component (along the stretching direction), thus causing very high local strain gradients. In fact, in these areas, the bending of the polymer is maximized by its alignment with the principal stretch direction causing a high strain localization. Moreover, the strong curvature and strain localization are usually harder measuring conditions for a stereoscopic DIC setup making these curves more prone to noise/discontinuities or lack some points at high strains.

Overall, the qualitative trends do not change with different polymer thicknesses or applied stretch levels even if the strain levels reached at the plateau are instead dependent on both parameters (as can be seen in table 2, the textile contracts more for higher pre-stretch/lower thickness values). The overall difference in trends between the 8-arm star structure and the 3-arm star pattern, is instead mainly caused by the fact the examined 3-arm star pattern bends locally at first and then slowly undergoes a minor macroscopical curvature, while the 8-arm star structure, being more massive and extending

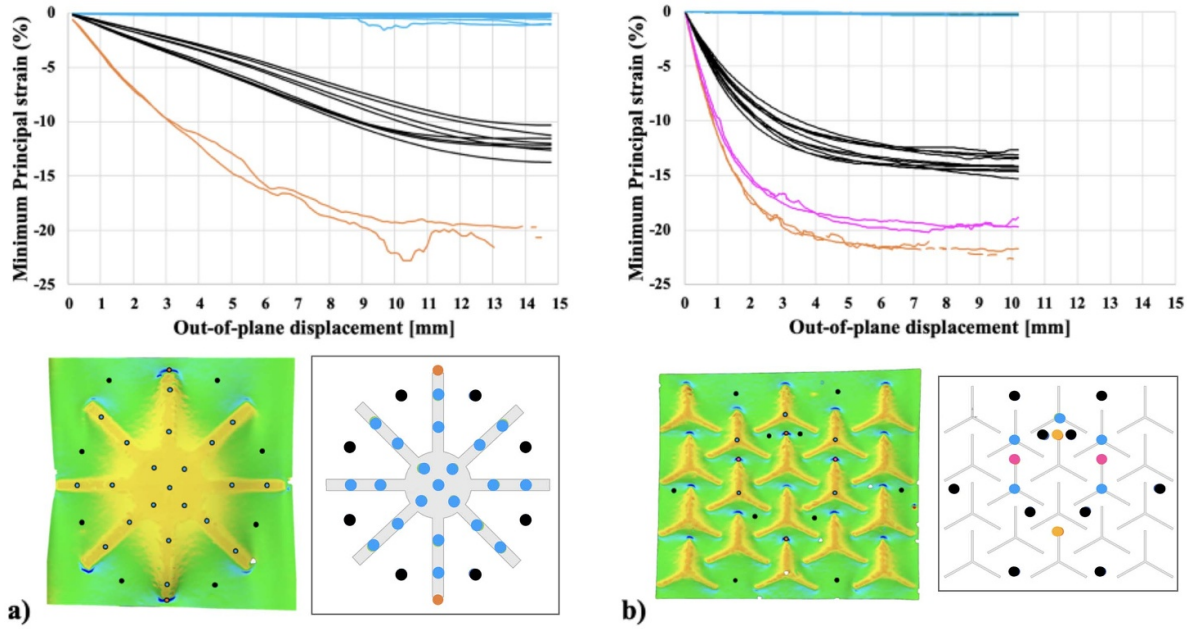

Figure 8. Evolution of the minimum principal strain as a function of displacement along z for (a) 8-arm star specimen with printed thickness equal to 0.3 mm and pre-stretch equal to 20%, and for (b) 3-arm star pattern specimen with printed thickness equal to 0.3 mm, pre-stretch equal to 20% and intermediate distance between printed elements. Cyan curves refer to points on the printed polymer; black curves refer to points on the fabric; orange and pink curves refer to the border areas between polymer and fabric, as shown in the mapping below each plot: each marker is coloured with the corresponding curve colour and the underlying mapping is displayed to facilitate recognizing fabric and polymer boundaries.

Table 2. Average minimum values (or plateau values) of the minimum principal strain for various types of configurations, pre-stretch, and thickness, for points on the printed polymer, points on the fabric, and points on the border areas between polymer and fabric; reported values were averaged on the various points.

Specimen	On the printed polymer	On the fabric	At the polymer/fabric border
Star–pre-stretch: 10%–thickness: 0.3 mm	0%	−10%	−18%
Star–pre-stretch: 20%–thickness: 0.3 mm	0%	−12%	−25%
Pattern–inter-distance: 8.5 mm–pre-stretch: 20%–thickness: 0.3 mm	0%	−14%	−28%
Pattern–inter-distance: 8.5 mm–pre-stretch: 40%–thickness: 0.3 mm	0%	−20%	−38%
Pattern–inter-distance: 8.5 mm–pre-stretch: 60%–thickness: 0.3 mm	−1%	−26%	−39%
Pattern–inter-distance: 8.5 mm–pre-stretch: 20%–thickness: 1.5 mm	−2%	−11%	−21%
Pattern–inter-distance: 8.5 mm–pre-stretch: 40%–thickness: 1.5 mm	−2%	−19%	−30%

through the whole specimen, leads to a slow and steady overall bending with the centre of the star moving more and more out-of-plane.

3.4. 8-arm star structure

The shapes assumed by the 8-arm star specimens for various textile pre-stretch and PLA thickness values are shown in figure 9(a) as top-view pictures, together with some examples of 3D scans; a different colour background was associated to the various pictures so to group together the different type of shapes assumed. These data give an idea of the different degree of curvature obtained for the various combinations of parameters. As expected, reducing thickness, and increasing pre-stretch often leads to greater curvatures. Specifically, by varying the values of these two parameters, different groups of equilibrium shapes can be observed. The shapes obtained may be classified in three principal situations: (i) a flat shape, with no curvature, typically observed when there is low pre-stretch or high thickness (blue region in figure 9(a)); (ii) regular dome-like shapes with varying degrees of curvature, usually obtained when the parameter values are in the intermediate range (yellow region); (iii) highly curved shapes that wrap around themselves, obtained when there is high pre-stretch and low thickness (red region). The 3D scans reported in figure 9(a) well depict such a variable behaviour.

Notably, only thicknesses of 0.9 mm or less result in a tangible alteration of shape when systems are removed from the

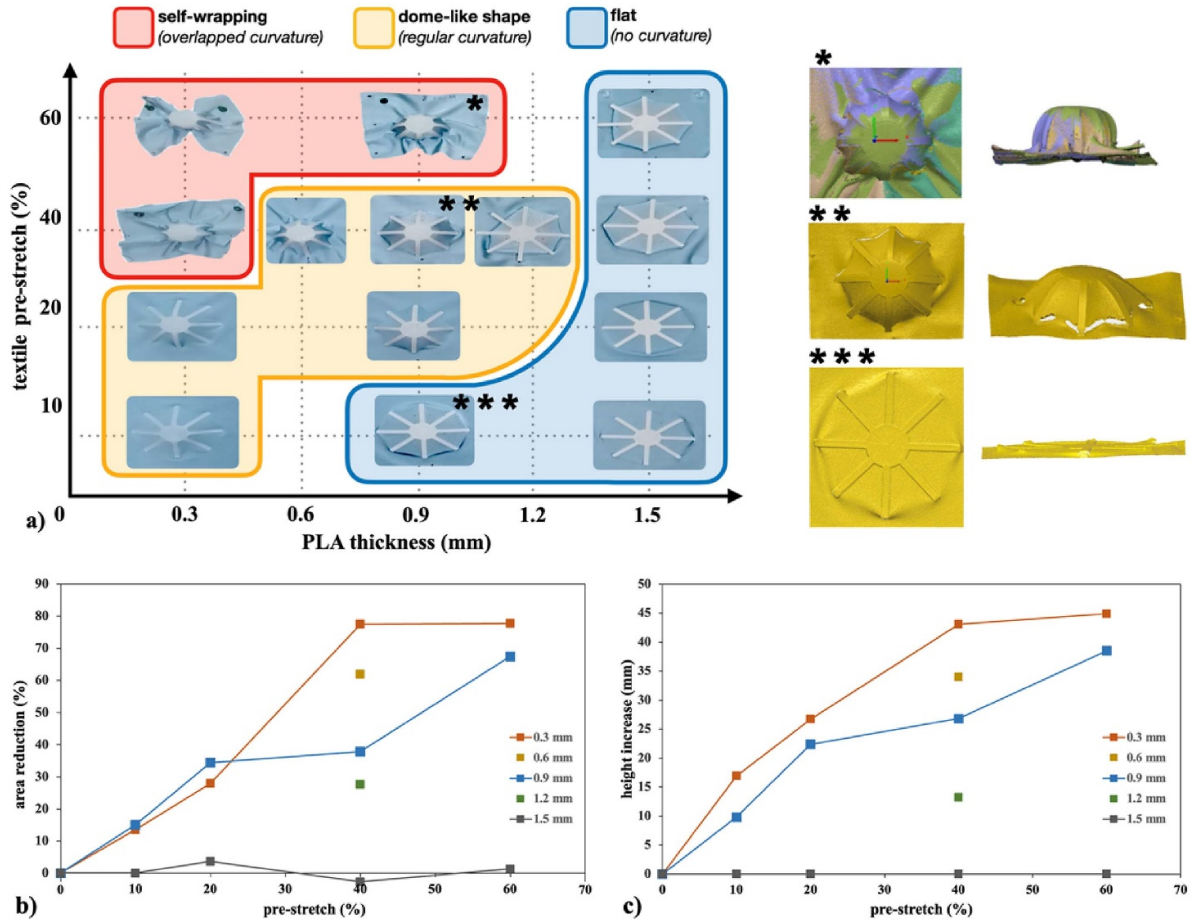

Figure 9. (a) Top-view appearance of the 8-arm star configuration after removal from the frame for various textile pre-stretch and PLA thickness values; details: 3D scan of samples with thickness 0.9 mm and different pre-stretch (*: 60%; **: 40%; ***: 10%). Evaluation of (b) area reduction and (c) height increase as a function of the tensile pre-stretch for various PLA thickness values.

frame. Additionally, within this range, the curvature is significantly affected by the amount of pre-stretch applied. In particular, a thickness of 0.9 allows for a variety of effects, ranging from minimal changes in shape (pre-stretch: 10%) to a uniform curvature (pre-stretch: 20%, 40%), and eventually to the capability of wrapping around itself (pre-stretch: 60%). By contrast, for very thick specimens no change of shape is detected.

These results, when compared to earlier investigations, merely confirmed that, as one could expect, greater pre-stretching and reduced thickness of the printed components result in increased curvatures. However, by systematically varying thickness and pre-stretch, we were able to accurately identify and analyze the different types of self-assembled curvature and establish a correlation with certain combinations of design factors. Similar maps, or 'phase diagrams' (as in Guiducci *et al* [22]), were shown in experimental and analytical studies for different types of geometries (undulated rods [22]; square grid [23]), facilitating the correlation between various types of curvature (flat; regular; unstable; multi-stable) and the conditions that promoted it. This kind of representation is considered essential for gaining a deeper comprehension of the behaviour and potential of 4D textiles, as well as for providing guidance in the design process for self-assembly.

To quantify the effect of the parameters on shape variation, two separate metrics were defined and assessed for the final 3D structure: the overall reduction of its projected area with respect to the initial stretched configuration, evaluated as percent variation through equation (1), and the rise in its height. The data were evaluated by means of an image analysis software and were found in good agreement with those measured by 3D scans on selected samples. Area reduction and height increase are depicted in figures 9(b) and (c), respectively, as a function of the textile pre-stretch and for various thicknesses. The curves demonstrate a consistent relationship between pre-stretch and the two output parameters for each thickness. For PLA thickness values of 1.5 mm or higher (2 mm; 3 mm), the 4D textiles do not exhibit any area reduction or height increase. By contrast, the thinnest systems (thickness = 0.3 mm) significantly change area and height when the pre-stretch rises from 10% to 20% to 40%, from which onwards the two metrics reach a plateau, as the 4D textiles show the self-wrapped configuration.

Intermediate combinations of thickness and pre-stretch generally show regular curvature and thus allow to control more easily the dome area and height.

The thickness of the printed elements governs their flexural stiffness, and for thickness values of 1.5 mm or higher

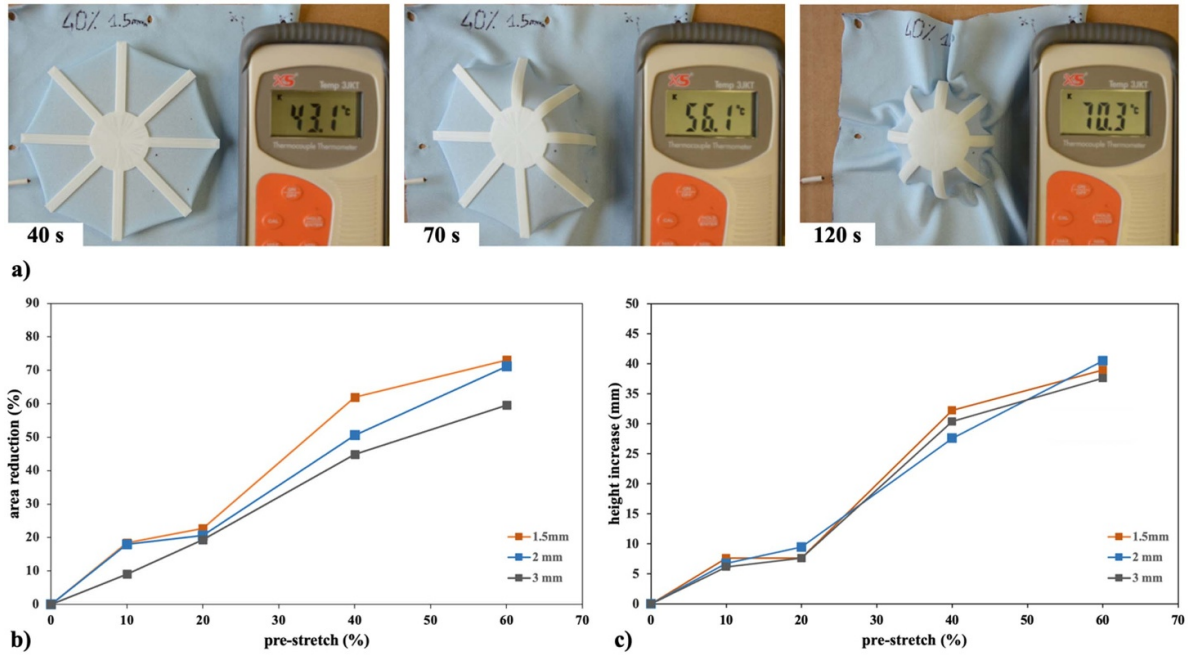

Figure 10. (a) Thermal activation of the shape transformation along a non-isothermal heating above T_g; evaluation of (b) area reduction and (c) height increase as a function of the tensile pre-stretch for various PLA thickness values.

the final equilibrium shape is completely governed by the stiff printed part, so that when the textile is removed from the frame it maintains a flat shape, even for the highest pre-stretch level (60%). However, in these systems, it was possible to significantly reduce the printed element stiffness by heating the material above PLA T_g (i.e. 65 °C), causing a decrease in PLA elastic modulus down to a few MPa, according to DMA results. This modifies the equilibrium state between the cloth and PLA, activating a shape change towards a curved configuration, as testified by the frames in figure 10(a) and by Mov 3 provided in the Supplementary Material.

Remarkably, the material maintains its flat state until approaching temperature close to the glass transition, after which it undergoes a transformation, generally on a timescale of 10–30 s; in order to visualize the phenomenon, the three pictures of figure 5(a) were recorded on a specimen triggered by means of a non-isothermal heating, referring to instants at temperature well below T_g (left picture), when approaching T_g (central picture), and when transformation is over (right picture).

The final shape of systems with thick printed elements (thickness = 1.5 mm, 2 mm, and 3 mm) was evaluated after having heated them to temperatures exceeding T_g (in an oven at 80 °C) and measuring the percentage reduction in area and the rise in height obtained, which are reported as a function of the pre-stretch in figures 10(b) and (c), respectively. The findings suggest that for these systems the pre-stretch has a greater influence than thickness, since the flexural stiffness is more influenced by the change in temperature than by the change in thickness, at least for the values of thickness here explored.

3.5. 3-arms star pattern structure

A similar approach was repeated for all the 3-arm star pattern, printed on variously pre-stretched textiles, and varying both thickness and mutual distance of the printed elements. Results concerning the shape displayed after stretch release are shown, as top-view images, in figure 11(a), where the shapes obtained are shown as top-view pictures, for the various pre-stretches, PLA thicknesses and mutual distances; a different colour background was associated to the various pictures were tentatively traced so to group together the different type of shapes assumed. The sets of behaviour displayed may be classified as four types: (i) structures that remain flat (blue region in figure 11(a)); (ii) structures that undergo curvature due to the cooperative action among the elements (yellow regions); (iii) structures whose curvature regards only the individual star-shaped element and does not involve any cooperation (green region); (iv) double curved structures, presenting both an overall curvature due to cooperative effects and an additional curvature of the individual elements (red region).

Flat structures are obtained only in the case of lowest pre-stretch and highest thickness, independently of the mutual element distance; conversely, the double curvature usually regards the cases of small thickness and high pre-stretch.

The remaining cases show either a cooperative effect of the elements in raising the structure in a regularly curved dome structure or a mutually non-influenced curvature of the single elements. By modifying the mutual distance of the elements, one can significantly modify the extent of the areas characterised by cooperative and non-cooperative curvature, as evidenced in the maps of figure 11(a). Having the elements close one to the other increases the likelihood of cooperative effect,

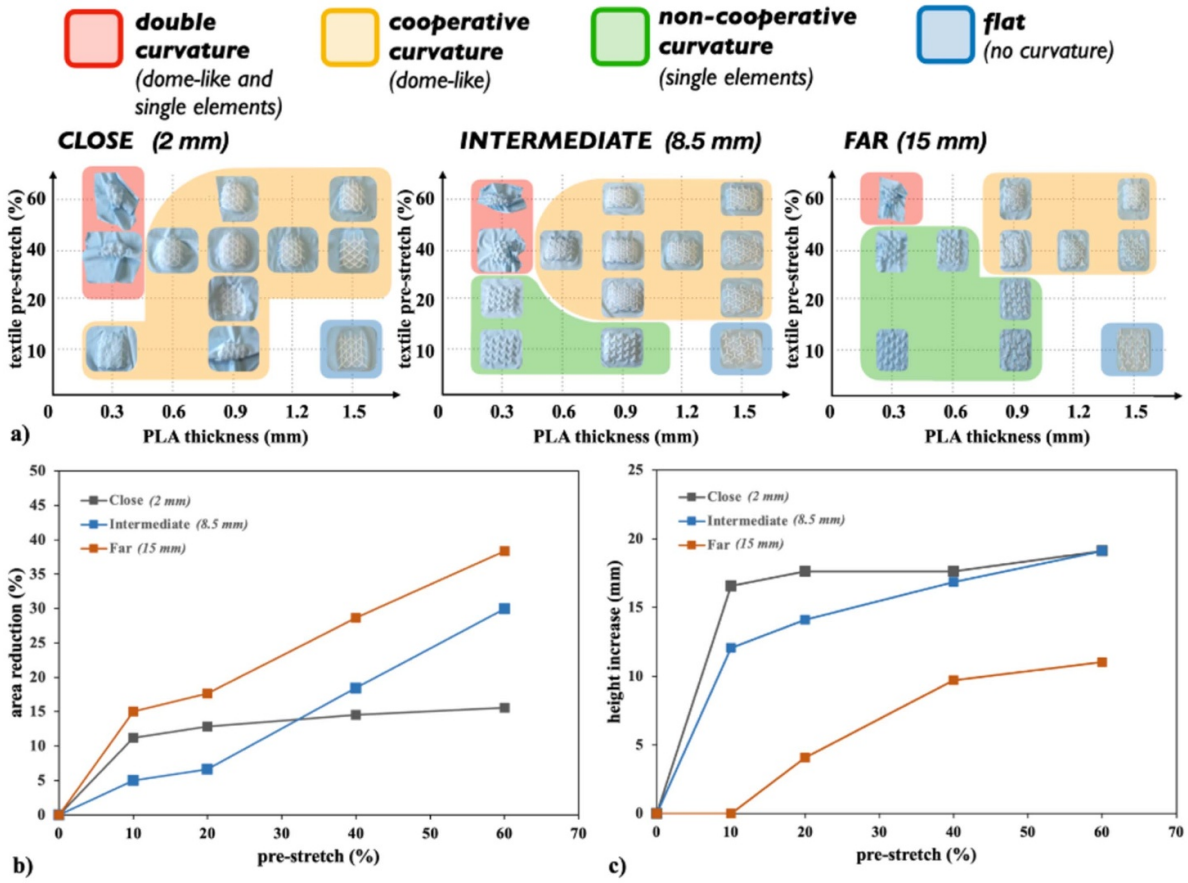

Figure 11. (a) Top view appearance of the 3-arm star pattern configuration after removal from the frame for various values of PLA thickness, textile pre-stretch and star inter-distance; evaluation of (b) area reduction and (c) height increase as a function of the tensile pre-stretch for thickness = 0.9 mm and the three inter-distance values (close: 2 mm; intermediate: 8.5 mm; far: 15 mm).

so that when elements are at the lowest mutual distance there are no cases of non-cooperative curvature; by contrast, greater mutual distance typically results in non-cooperative curvature of individual elements.

The values of area reduction and the height increase were also evaluated and reported in figures 11(b) and (c), respectively, for selected examples (specimens with thickness of 0.9 mm and three different inter-distance values); the values measured for other specimen thickness values (0.3 mm and 1.5 mm) are reported as Supplementary Materials (figure S6), showing maximum height increase equal to 30 mm and maximum area decrease equal to 60% for the thinnest 3D printed elements and the highest pre-stretch.

The results still confirm the possibility of controlling the amount of curvature and height by varying pre-stretch and thickness: area reduction and height increase are smaller for when the printed structure is thicker, and they both increase with pre-stretch. The additional parameter, represented by the mutual distance, affects the area reduction so that larger contractions are found for more distanced elements. The height increase has a more complex dependence on mutual distance: in fact, it is shown that the closer the elements, the larger is the possibility of cooperation and height increase even at low pre-stretch; for all the thicknesses an upper value for the height increase is suggested, and this maximum height seems to become higher for thinner elements.

Overall, it is shown that the far configuration allows more area reduction but does not help in increasing height; the close one, on the other hand, allows to enhance height, but the contraction is hindered by the elements touching each other; finally, the intermediate case allows a more regular control of both parameters. However, the trends highlighted by the curves may look less regular with respect to those found for the 8-arm star structure, because of the more complex scenario investigated and the various types of curved structures that are obtained.

Furthermore, a statistical investigation was carried out on the results of figure 11. The analysis was conducted with two objectives. The first aims at identifying which and how design parameters (fabric pre-stretch, PLA thickness and elements inter-distances influence the variation in the projected area of 3-arm star patterns; the other aims at defining a numerical regression model that expresses with sufficient precision the influence of such parameters on the final response. The analysis was carried out by means of the software Minitab. Several polynomial regression models were considered in the analysis and the optimal model (i.e. the polynomial which uses the least number of statistically

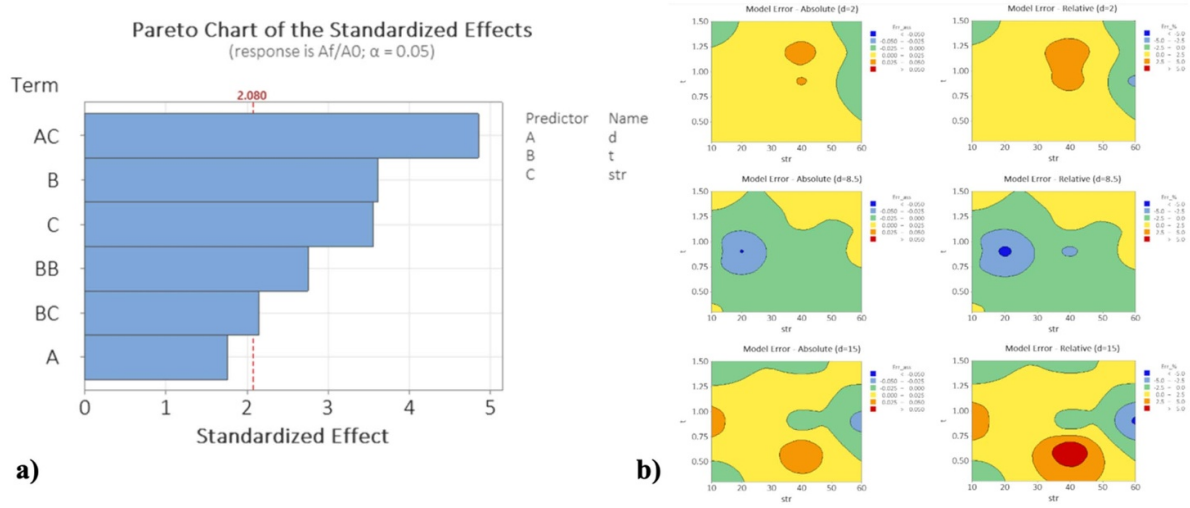

Figure 12. (a) Pareto chart of the influencing parameters included in the model (d = elements inter-distance, t = PLA thickness, str = textile pre-stretch). Not influencing terms (i.e. the parameter d) were included based on the hierarchical principle [58]; (b) absolute error (left) and relative error (right) of the regression model as a function of thickness (t), pre-stretch (str) and element inter-distance (d).

significant terms) was identified. Accordingly, the BIC estimator (Bayesian Information Criterion) [57] and F-test were adopted. BIC was used to rank the considered regression models and to exclude those which overfit the experimental data by using a higher number of terms; the finally employed equation can be written as:

$$\frac{A_{\text{after}}}{A_{\text{in}}} = 0.8624 - 0.00357d + 0.2620t - 0.00402\text{str} - 0.1146t \cdot t - 0.000244d \cdot \text{str} + 0.001719t \cdot \text{str} \quad (4)$$

where A_{after} and A_{in} represents the projected area after and before the stretch release, d is the interdistance, t is the thickness and str is the pre-stretch.

Furthermore, F-test was used to confirm the statistical influence of the parameters included in the optimal regression model (i.e. p-value lower than 0.05). Based on the statistical analysis carried out, it can be confirmed that the parameters studied (pre-stretch, thickness, and inter-distance) and their interactions statistically influence the variation in the area of the analysed samples (Pareto chart in figure 12(a)).

The precision of the model was evaluated in terms of error as the difference between the model and the experimental data. Figure 12(b) reports the Contour Plots of the model precision in terms of absolute and relative error, which were mapped as a function of thickness, pre-stretch, and element inter-distance. The error maps show that the deviation between the obtained model and the real data is overall small, with a percentage error generally varying in a range of ±2.5%, with a few isolated values reaching an error percentage of ±5%.

Overall, through the statistical analysis of the variation in area as a function of the design parameters, it was possible to confirm these strong correlations at an analytical level. Exploring this aspect of research would make it possible to obtain models for quantified predictions of the 4D textile shapeshifting behaviour for a variety of combinations of the design parameters.

3.6. Adhesion tests

Another aspect verified regards the adhesion between the printed layers and the textile support, which is expected to play a crucial role in the stability of the structure, and thus in maintaining effective the shape-shifting behaviour.

The strength of this bond and the local adhesion may in fact influence the stress state of the system, as well as the repeatability of the shape-shifting process, the overall reliability of the structure, and the durability of the deformed structure.

The adhesion was verified by the application of the 180° T-peel test methodology, which involves the measurement of the force required to peel the pre-stretched fabric from the printed polymer. In particular, the tests were carried out on bars printed on variously pre-stretched textiles (pre-stretch: 10, 20, 30, 40%) along various directions with respect to the wale direction (0°, 90° and 45°, i.e. parallel, perpendicular and at 45° with respect to the wale direction, respectively), and repeated three times for each condition.

The typical results obtained are depicted in figure 13(a) in the case of bars printed along the 0° direction and for the various pre-stretch values (one representative curve for each pre-stretch was selected). The curves illustrate the force, normalised to the printed element width, necessary to separate the two materials as the crosshead displacement is gradually increased. The curves exhibit a pattern of scattered peaks and valleys, indicating a non-uniform peeling process until full delamination. No discernible relationship is found between the progressive displacement and the measured strength. Indeed, the results show that interfacial strength assumes various and highly localised values, so that the same sample might exhibit areas of strong adhesion near regions of weak adhesion. Specifically, the borders appear to be prone to delamination, likely because of the significant constraint and interfacial stress localization on the textile in these areas. Additionally, a statistical distribution of local interfacial strength values was observed, likely due to random factors such as the lack of a

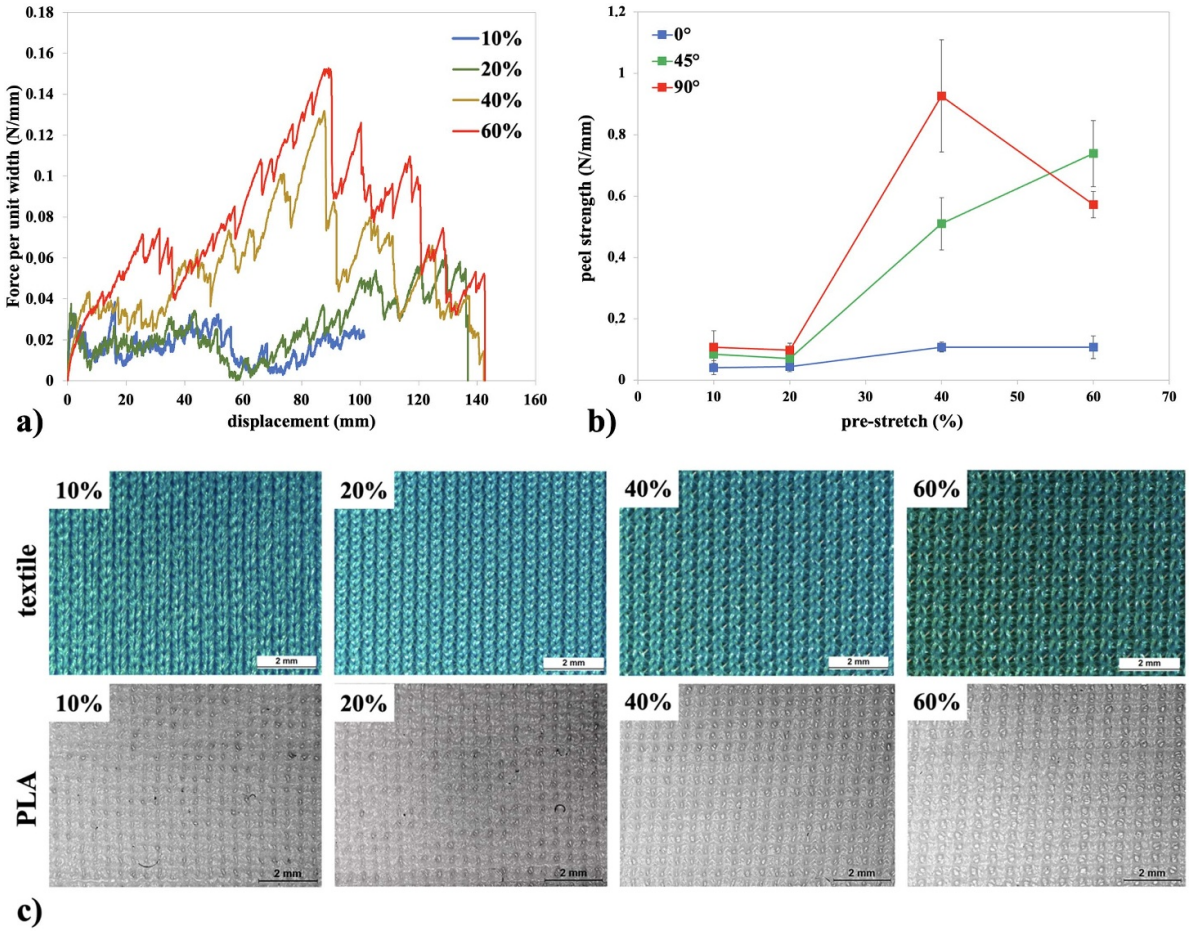

Figure 13. (a) Force per unit width vs. displacement curves for the specimens printed along the wale direction (0°) on fabric with various levels of pre-stretch; (b) peel strength (average peak force per unit width) for various pre-stretch values and printing directions; (c) appearance of the textile at various stretching and of the printed PLA surface facing the fabric after peeling, for specimens printed along the wale direction and with various levels of textile pre-stretch.

perfectly flat printing plane and the non-uniform pre-stretch of the textile.

However, an overall value for the interfacial strength of the various systems was arbitrarily provided as the average of the 10 highest normalised force peaks. It should be noted that this assessment of strength only considers the highest values of local adhesion, as it does not take into account the distribution of lower peaks and their corresponding values. These values results are depicted in figure 13(b) for the various pre-stretch levels and for the three printing directions. Despite the notable dispersion, the findings indicate that both pre-stretching and printing direction contribute to PLA-fabric adhesion. Higher pre-stretch values lead to statistically significant increments in adhesion peaks, for specimens printed at 45° and 90°, which show the highest adhesion values. These findings might be attributed to the fact that adhesion is promoted by a hook-and-loop interaction between the polymer, solidified as sort of micro-pillars in the pores of the fabrics, and the textile mesh. In fact, when the fabric is stretched, larger space is provided for the printed polymer to interact. As the textile pictures in figure 13(c) suggest, such space assumes the shape of small pores for the lowest pre-stretch levels (10%; 20%), and of larger lines at higher pre-stretch. Because of this morphology, the polymer penetration gets more effective as pre-stretch increases, evolving from grids of small pillars to larger pillars, organized in long lines, and with increased contact surface with the textile. This increased surface-to-volume ratio ultimately justifies the significant increase of average peel strength measured at all angles, and for pre-stretch equal to 40% or higher. The textile morphology under stretching at various strain levels seems to also govern the difference in peel strength along the various directions; in fact, reasonably, peeling occurs more easily along the free space lines (0°), while adhesion becomes higher when peeling takes place across them (45°, 90°).

However, it is important to remark that, despite the widely dispersed strength values and all the problems related to adhesion promotion (its highly local nature; the presence of a large set of weak points; the difficulties in controlling and homogenising the interfacial strength), all the 4D textiles here described always exhibited adequate adhesion to ensure the pieces remained attached during shape changes, suggesting

that the conditions to adequately connect textile and PLA so to withstand the out-of-plane curvature were easily met in all conditions.

4. Conclusion

An empirical study was developed to highlight the relationships between the realisation parameters of 4D textiles and their shapeshifting response. The results allowed the identification of specific peculiarities of their shape evolution upon stress release.

The shape assumed is strongly dependent on the printed geometry, being not only dictated by the equilibrium state between the printed element and the area in direct contact with it, but also by the stress and strain state developed in the region surrounding the printed area. In fact, DIC results revealed a bimodal state of strain in the final state of the shape transformations: a relevant part of strain resides in the regions of textile between printed elements, which, by contrast, do not deform axially, but display a significant out-of-plane curvature.

At the tension release, all the systems underwent a curvature which was strongly affected by the combination of the analysed parameters, and displayed a very wide range of equilibrium shapes: from the degenerate case of no curvature (typically for low pre-tension and high thickness, where the bending stiffness of PLA prevents the pre-stretch from exerting curvature) to various curved-shape scenarios, i.e. formation of dome-like structures, cooperative/non-cooperative bending, and self-wrapping (this latter case shown for high pre-stretch and low thickness). Regular dome-like shapes may be assumed only for specific combinations of pre-stretching, thickness, and inter-distance of printed elements. Overall, it was shown that curvature increases with the applied pre-stretch, and it decreases for thicker, and thus stiffer, printed patterns, while showing a more complex dependence on the inter-distance, strongly affecting the cooperative/non-cooperative nature of the bending phenomena. These findings were described through correlation maps as well as a polynomial regression model, that could be exploited for guiding the design of the 4D textiles and tailoring their final shape. Moreover, thickness may be used to temporarily fix a flat shape whose shift may be activated by heating above T_g, paving the way to novel types of thermally triggered 4D textiles, whose response may be remotely activated or delayed in time.

Finally, the investigation on adhesion among the printed elements and the carrier surface revealed a highly local nature of the delamination failure, so that the interfacial strength distribution may strongly change from region to region of the same printed bar. However, it is highlighted that the maximum values of strength are usually achieved for textiles subjected to a higher pre-stretch and for printing directions perpendicular or at a certain angle with respect to the wale direction, because of the higher interfacial surface developed when the printed polymer penetrates the textile pores. Importantly, despite their highly distributed peel strength values, all the specimens revealed a sufficient adhesion to maintain the elements connected during shape transformations and to exhibit the expected flexural effects.

Data availability statement

All data that support the findings of this study are included within the article (and any supplementary files).

Acknowledgments

The authors would like to express their gratitude to the students who contributed to the experimental activities, for their constant efforts and the discussion of the results: Mr Stefano Zanelli, Mr Claudio Cominelli, Mr Simone Ermici, Mr Leo-Paul Legrand.

ORCID iDs

Stefano Pandini https://orcid.org/0000-0003-2390-8495
Chiara Pasini https://orcid.org/0000-0001-7478-239X
Davide Battini https://orcid.org/0000-0002-2044-5985
Andrea Avanzini https://orcid.org/0000-0002-7188-7687
Antonio Fiorentino https://orcid.org/0000-0002-9439-7074
Ileana Bodini https://orcid.org/0000-0003-4904-2044
Simone Pasinetti https://orcid.org/0000-0002-5098-6395

References

[1] Alshebly Y S, Nafea M, Mohamed Ali M S and Almurib H A F 2021 Review on recent advances in 4D printing of shape memory polymers *Eur. Polym. J.* **159** 110708
[2] Lee A Y, An J and Chua C K 2017 Two-way 4D printing: a review on the reversibility of 3D-Printed shape memory materials *Engineering* **3** 663–74
[3] Wang L L, Zhang F H, Du S Y and Leng J S 2023 Advances in 4D printed shape memory composites and structures: actuation and application *Sci. China Technol. Sci.* **66** 1271–88
[4] Khalid M Y, Arif Z U, Noroozi R, Zolfagharian A and Bodaghi M 2022 4D printing of shape memory polymer composites: a review on fabrication techniques, applications, and future perspectives *J. Manuf. Process.* **81** 759–97
[5] Champeau M *et al* 2020 4D printing of hydrogels: a review *Adv. Funct. Mater.* **30** 1910606
[6] Chalissery D, Schönfeld D, Walter M, Ziervogel F and Pretsch T 2022 Fused filament fabrication of actuating objects *Macromol. Mater. Eng.* **307** 2200214
[7] Rajkumar A R and Shanmugam K 2018 Additive manufacturing-enabled shape transformations via FFF 4D printing *J. Mater. Res.* **33** 4362–76
[8] Chalissery D, Schönfeld D, Walter M, Shklyar I, Andrae H, Schwörer C, Amann T, Weisheit L and Pretsch T 2022 Highly shrinkable objects as obtained from 4D printing *Macromol. Mater. Eng.* **307** 2100619
[9] Goo B, Hong C H and Park K 2020 4D printing using anisotropic thermal deformation of 3D-printed thermoplastic parts *Mater. Des.* **188** 108485

[10] Ramezani M and Mohd Ripin Z 2023 4D printing in biomedical engineering: advancements, challenges, and future directions *J. Funct. Biomater.* **14** 347

[11] Sajjad R, Chauhdary S T, Anwar M T, Zahid A, Khosa A A, Imran M and Sajjad M H 2024 A review of 4D printing—technologies, shape shifting, smart polymer-based materials, and biomedical applications *Adv. Ind. Eng. Polym. Res.* **7** 20–36

[12] Niazy D, Ashraf M, Bodaghi M and Zolfagharian A 2024 Resilient city perspective: 4D printing in art, architecture and construction *Mater. Today Sustain.* **26** 100708

[13] Soleimanzadeh H, Rolfe B, Bodaghi M, Jamalabadi M, Zhang X and Zolfagharian A 2023 Sustainable robots 4D printing *Adv. Sustain. Syst.* **7** 2300289

[14] Franco Urquiza E A 2024 Advances in additive manufacturing of polymer-fused deposition modeling on textiles: from 3D printing to innovative 4D Printing—A review *Polymers* **16** 700

[15] Manaia J P, Cerejo F and Duarte J 2023 Revolutionising textile manufacturing: a comprehensive review on 3D and 4D printing technologies *Fashion Text.* **10** 20

[16] Li S 2023 Review on development and application of 4D-printing technology in smart textiles *J. Eng. Fibers Fabrics* **18** 1–18

[17] Du W, Ren H, Xu W and Liu Y 2024 Reversible shape memory behavior of knitting-fabric reinforced polymer matrix composites *Comput. Commun.* **48** 101962

[18] Huang Y, Ren H, Liu Y, Xu W and Zhao W 2024 Bending shape memory properties and multi-scale viscoelastic behaviors of knitted-fabric reinforced polymer composites *Comput. Sci. Tecnnicol.* **256** 110747

[19] Khan M R K and Hassan M N 2021 Understanding the concept of 4D textiles *South Asian Res. J. Eng. Technol.* **3** 93–95

[20] Koch H C, Schmelzeisen D and Gries T 2021 Textiles made by additive manufacturing on pre-stressed textiles—An overview *Actuators* **10** 1031

[21] Zhang J, Shen D, Yu Y, Bao D, Li C and Qin J 2024 Direct-print thermally responsive 4D textilescby depositing PLA on prestretched fabrics *Rapid Prototyp. J.* **30** 277–86

[22] Guiducci L, Kycia A, Sauer C and Fratzl P 2022 Self-organized rod undulations on pre-stretched textiles *Bioinspir. Biomim.* **17** 036007

[23] Stapleton S E, Kaufmann D, Krieger H, Schenk J, Gries T and Schmelzeisen D 2019 Finite element modeling to predict the steady-state structural behavior of 4D textiles *Text. Res. J.* **89** 3484–98

[24] Zhang W, Zhang F, Lan X, Leng J, Wu A S, Bryson T M, Cotton C, Gu B, Sun B and Chou T W 2018 Shape memory behavior and recovery force of 4D printed textile functional composites *Compos. Sci. Technol.* **160** 224–30

[25] Schmidt A M, Schmelzeisen D and Gries T 2022 4D-textiles: development of bistable textile structures using rapid prototyping and the bionic approach *Rapid Prototyp. J.* **28** 1589–97

[26] Leist S K, Gao D, Chiou R and Zhou J 2017 Investigating the shape memory properties of 4D printed polylactic acid (PLA) and the concept of 4D printing onto nylon fabrics for the creation of smart textiles *Virtual Phys. Prototyp.* **12** 290–300

[27] Neuß J, Kreuziger M, Grimmelsmann N and Korger M, Ehrmann A 2016 Interaction between 3D deformation of textile fabrics and imprinted lamellae *Proc. Int. Textile Conf. Dresden* pp 24–25

[28] Otto F and Rasch B 1995 *Finding Form: Towards an Architecture of the Minimal* (Axel Menges Editions)

[29] Liang H and Mahadevan L 2009 The shape of a long leaf *Proc. Natl Acad. Sci. USA* **106** 22049–54

[30] Pocivavsek L, Dellsy R, Kern A, Johnson S, Lin B, Lee K Y C and Cerda E 2008 Stress and fold localization in thin elastic membranes *Science* **1979** 912–6

[31] Sharon E, Roman B, Marder M, Shin G S and Swinney H L 2002 Buckling cascades in free sheets *Nature* **419** 579

[32] Clasen D, Wallasch M and Köneke O 2017 Sonogrid (available at: http://sonogrid.de/konzept/) (Accessed 27 April 2017)

[33] Guberan C and Clopath C Self-assembly lab active shoes (available at: https://selfassemblylab.mit.edu/active-shoes) (Accessed 20 June 2024)

[34] Schmelzeisen D, Koch H, Pastore C and Gries T 2018 4D textiles: hybrid textile structures that can change structural form with time by 3D Printing *Narrow Smart Textiles* ed Kyosev Y, Mahltig B and Schwarz-Pfeiffer A (Springer) 189–201

[35] Kicia A Material form-finding of modular textile structures (available at: https://ca2re.eu/wp-content/uploads/2020/08/Aarhus-2018-Kycia-full-paper.pdf) (Accessed 20 June 2024)

[36] Barletta M, Gisario A and Mehrpouya M 2021 4D printing of shape memory polylactic acid (PLA) components: investigating the role of the operational parameters in fused deposition modelling (FDM) *J. Manuf. Process.* **61** 473–80

[37] Miao S, Zhu W, Castro N J, Nowicki M, Zhou X, Cui H, Fisher J P and Zhang L G 2016 4D printing smart biomedical scaffolds with novel soybean oil epoxidized acrylate *Sci. Rep.* **6** 61–10

[38] Ahrendt D and Romero Karam A 2020 Development of a computer-aided engineering–supported process for the manufacturing of customized orthopaedic devices by three-dimensional printing onto textile surfaces *J. Eng. Fibers Fabr.* **15** 1–11

[39] Agkathidis A, Berdos Y and Brown A 2019 Active membranes: 3D printing of elastic fibre patterns on pre-stretched textiles *Int. J. Archit. Comput.* **17** 74–87

[40] Agkathidis A and Varinlioglu G 2022 4D printing on textiles: developing a file to fabrication framework for self-forming, composite wearables *Advances in Product Design Engineering* ed Kyratsis P, Efkolidis N and Davim J (Springer) pp 61–81

[41] Pérez J, Otaduy M.A and Thomaszewski B 2017 Computational design and automated fabrication of kirchhoff-plateau surfaces *ACM Trans. Graph.* **36** 1–12

[42] Malengier B, Hertleer C, Cardon L, Van Langenhove L and Reynders D 2018 3D printing on textiles: testing of adhesion *Fashion Technol. Text. Eng.* **S4** 1–4

[43] Sitotaw D B, Ahrendt D, Kyosev Y and Kabish A K 2020 Additive manufacturing and textiles—state-of-the-art *Appl. Sci.* **10** 5033

[44] Narula A, Pastore C M, Schmelzeisen D, Basri S E, Schenk J and Shajoo S 2018 Effect of knit and print parameters on peel strength of hybrid 3-D printed textiles *J. Text. Fibrous Mater.* **1** 1–10

[45] Grimmelsmann N, Kreuziger M, Korger M, Meissner H and Ehrmann A 2018 Adhesion of 3D printed material on textile substrates *Rapid Prototyp. J.* **24** 166–70

[46] Hashemi Sanatgar R, Campagne C and Nierstrasz V 2017 Investigation of the adhesion properties of direct 3D printing of polymers and nanocomposites on textiles: effect of FDM printing process parameters *Appl. Surf. Sci.* 403 551–63

[47] Sabantina L, Kinzel F, Ehrmann A and Finsterbusch K 2015 Combining 3D printed forms with textile structures—mechanical and geometrical properties of multi-material systems *IOP Conf. Ser.: Mater. Sci. Eng.* **87** 012005

[48] Eutionnat-Diffo P A, Chen Y, Guan J, Cayla A, Campagne C, Zeng X and Nierstrasz V 2020 Optimization of adhesion of

poly lactic acid 3D printed onto polyethylene terephthalate woven fabrics through modelling using textile properties *Rapid Prototyp. J.* **26** 390–401
[49] Kozior T, Blachowicz T and Ehrmann A 2020 Adhesion of three-dimensional printing on textile fabrics: inspiration from and for other research areas *J. Eng. Fibers Fabr.* 15 377–80
[50] Spahiu T, Al-Arabiyat M, Martens Y, Ehrmann A, Piperi E and Shehi E 2018 Adhesion of 3D printing polymers on textile fabrics for garment production *IOP Conf. Ser.: Mater. Sci. Eng.* **459** 012065
[51] Meyer P, Döpke C and Ehrmann A 2019 Improving adhesion of three-dimensional printed objects on textile fabrics by polymer coating *J. Eng. Fibers Fabr.* **14** 1–7
[52] Tadesse M G, Dumitrescu D, Loghin C, Chen Y, Wang L and Nierstrasz V 2017 3D printing of ninjaflex filament onto PEDOT: PSS-coated textile fabrics for electroluminescence applications *J. Electron. Mater.* **47** 472082–92
[53] Pei E, Shen J and Watling J 2015 Direct 3D printing of polymers onto textiles: experimental studies and applications *Rapid Prototyp. J.* **21** 556–71
[54] Rivera M L, Moukperian M, Ashbrook D, Mankoff J and Hudson S E 2017 Stretching the bounds of 3D printing with embedded textiles *Conf. on Human Factors in Computing Systems—Proc.* pp 497–508
[55] Raise3D Premium PLA Technical Data Sheet 2022 (available at: https://s2.raise3d.com/public/media/2019/07/Raise3D_Premium_PLA_TDS_V4.pdf) (Accessed 20 June 2024)
[56] Yan D, Chang J, Zhang H, Liu J, Song H, Xue Z, Zhang F and Zhang Y 2020 Soft three-dimensional network materials with rational bio-mimetic designs *Nat. Commun.* **11** 1–11
[57] Burnham K P and Anderson D R 2022 *Model Selection and Multimodel Inference A Practical Information—Theoretic Approach* (Springer)
[58] Montgomery D C 2021 *Design and Analysis of Experiments, EMEA* 10th edn (Wiley)